The Astrophysical Journal, 881:108 (12pp), 2019 August 20
https://doi.org/10.3847/1538-4357/ab2dfe

New Constraints on the Dust and Gas Distribution in the LkCa 15 Disk from ALMA

Sheng Jin[1], Andrea Isella[2], Pinghui Huang[1,2,3,4], Shengtai Li[3], Hui Li[3], and Jianghui Ji[1,5]
[1] CAS Key Laboratory of Planetary Sciences, Purple Mountain Observatory, Chinese Academy of Sciences, Nanjing 210008, People's Republic of China
shengjin@pmo.ac.cn
[2] Department of Physics and Astronomy, Rice University, 6100 Main St., Houston, TX 77005, USA
[3] Theoretical Division, Los Alamos National Laboratory, Los Alamos, NM 87545, USA
[4] University of Chinese Academy of Sciences, Beijing 100049, People's Republic of China
[5] CAS Center for Excellence in Comparative Planetology, Hefei 230026, People's Republic of China
Received 2019 March 26; revised 2019 June 27; accepted 2019 June 28; published 2019 August 20

Abstract

We search a large parameter space of the LkCa 15's disk density profile to fit its observed radial intensity profile of ^{12}CO ($J = 3$–2) obtained from Atacama Large Millimeter/submillimeter Array. The best-fit model within the parameter space has a disk mass of 0.1 $M_\odot$ (using an abundance ratio of $^{12}\mathrm{CO/H_2} = 1.4 \times 10^{-4}$ in mass), an inner cavity of 45 au in radius, an outer edge at ∼600 au, and a disk surface density profile that follows a power law of the form $\rho_r \propto r^{-4}$. For the disk density profiles that can lead to a small reduced χ^2 of the goodness-of-fit, we find that there is a clear linear correlation between the disk mass and the power-law index, γ, in the equation of the disk density profile. This suggests that the ^{12}CO disk of LkCa 15 is optically thick, and we can fit its ^{12}CO radial intensity profile using either a lower disk mass with a smaller γ or a higher disk mass with a bigger γ. By comparing the ^{12}CO channel maps of the best-fit model with disk models with higher or lower masses, we find that a disk mass of ∼0.1 $M_\odot$ can best reproduce the observed morphology of the ^{12}CO channel maps. The dust continuum map at 0.87 mm of the LkCa 15 disk shows an inner cavity of the similar size of the best-fit gas model, but its outer edge is at ∼200 au, which is much smaller than the fitted gas disk. Such a discrepancy between the outer edges of the gas and dust disks is consistent with dust drifting and trapping models.

Key words: protoplanetary disks – radiative transfer – stars: individual (LkCa 15) – submillimeter: planetary systems

1. Introduction

Recently, a large number of protoplanetary disks were spatially resolved by the Atacama Large Millimeter/submillimeter Array (ALMA) and the Next Generation Very Large Array (ngVLA; ALMA Partnership et al. 2015; Fedele et al. 2017; Andrews et al. 2018; Isella et al. 2018; Liu et al. 2018b). These high-resolution observations of protoplanetary disks in dust continuum and molecular line emissions provide us the morphology of dust and gas distributions in a wide variety of protoplanetary disks. Such information places fundamental constraints for the theoretical studies on dust properties and dust–gas interaction, which is an important building block of planet formation theory (Dong et al. 2015, 2018; Isella et al. 2016; Jin et al. 2016; Huang et al. 2018; Liu et al. 2018a; Ricci et al. 2018; P. Huang et al. 2019, in preparation).

LkCa 15 is a 2–5 Myr old K5 star with $L_\star \sim 0.74\,L_\odot$ and $M_\star \sim 1.0\,M_\odot$ (Kenyon & Hartmann 1995; Simon et al. 2000). It is located in the Taurus-Auriga star-forming region at a distance of 140 pc from the Earth (van den Ancker et al. 1998). LkCa 15 is an interesting target due to its partially dust-depleted disk (Piétu et al. 2006; Espaillat et al. 2007; Thalmann et al. 2010, 2014; Andrews et al. 2011; Isella et al. 2012, 2014) and the probability of harboring a planet candidate inside its inner cavity (Kraus & Ireland 2012; Sallum et al. 2015; Thalmann et al. 2016; Currie et al. 2019). The depleted inner region shown in the dust continuum image is about 50 au in radius (Piétu et al. 2006; Andrews et al. 2011; Isella et al. 2012, 2014), and it has a mass accretion rate of about $10^{-9}\,M_\odot\,\mathrm{yr}^{-1}$ (Hartmann et al. 1998). The outer edge of the dust disk inferred from continuum emission is at ∼150 au (Piétu et al. 2007; Isella et al. 2012). The dust mass estimated from 1.3 mm continuum observation is about $5 \times 10^{-4}\,M_\odot$ (Isella et al. 2012). Recent images of scattered light suggest a warped inner disk component inside the inner gap, providing clear picture details of the inner gap region of the LkCa 15 disk (Thalmann et al. 2015, 2016; Oh et al. 2016).

As a young star, LkCa 15 is a luminous source of X-ray and extreme ultraviolet (EUV) emission (Skinner & Güdel 2013), indicating that the LkCa 15 disk could still be undergoing the active evolution phase of disk physics and chemistry. Consequently, the protoplanetary disk of LkCa 15 has been found to be especially chemically rich and has been detected in several molecular transitions (Thi et al. 2004; Piétu et al. 2007; Chapillon et al. 2008; Öberg et al. 2010; Punzi et al. 2015). Molecular line emission shows that the gas disk around LkCa 15 is the size of ∼900 au (Piétu et al. 2007; Isella et al. 2012). It is highly optically thick in the emission of ^{12}CO but is optically thin in ^{13}CO emission (Punzi et al. 2015; van der Marel et al. 2015). The discrepancy between the outer disk radii shown in the dust continuum and molecular line emissions (∼150 au versus 900 au) suggests that the mm-size dust is depleted in the outer part of the LkCa 15 disk, which is consistent with dust drifting and trapping models (Birnstiel et al. 2010; Pinilla et al. 2012).

Being a protoplanetary disk that may have a young planet candidate, the LkCa 15 system serves as a unique laboratory to study the dust evolution models under planet–disk interaction (Zhu et al. 2011; Pinilla et al. 2012). The distribution of dust and gas in the LkCa 15 disk provides an important constraint on theoretic models. Here, we fit the gas and dust surface density profiles based on the high-resolution dust continuum image and CO 3–2 line maps obtained from the ALMA. We study how the goodness-of-fit changes along with different key parameters used in the disk density profile, which is related

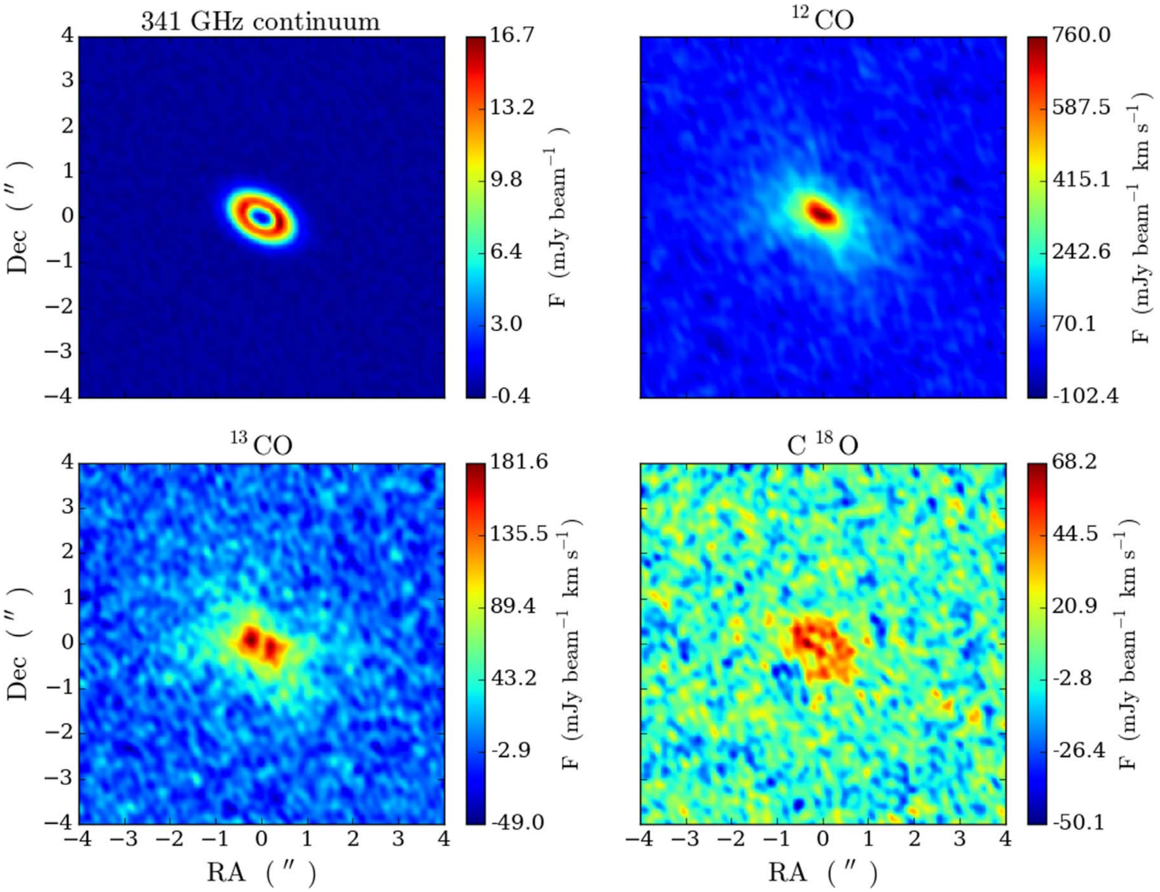

Figure 1. ALMA observations of the dust continuum, and zero-moment ^{12}CO, ^{13}CO, and C^{18}O maps of the LkCa 15 system. Top left: the dust continuum map. Top right: the zero-moment ^{12}CO map. Bottom left: the zero-moment ^{13}CO map. Bottom right: the zero-moment C^{18}O map.

with different physics. Our disk model and the parameter grid is described in Section 3. In Section 4, we show the best-fit model with respect to the observed ^{12}CO image. We discuss the dependence of the parameters in Section 5.

2. Observation

The LkCa 15 was observed on 2014 August 17 and 29 with ALMA Band 7 (345 GHz, 880 μm) in ALMA program 2012.1.00870.S (PI Pérez, L. M.). The ^{12}CO, ^{13}CO, and C^{18}O 3–2 line maps and 0.87 mm dust continuum image were taken with two different tunings. The ^{12}CO 3–2 data were obtained with a spectral window centered on 345.796 GHz with 1885 channels of 122.06 kHz (0.106 km s^{-1}) channel width. The angular resolution of the ^{12}CO image is 0.″36 × 0.″23 (50 au × 32 au). The ^{13}CO 3–2 data were centered on 330.588 GHz, with 1967 channels of 122.06 kHz (0.11 km s^{-1}) channel width. The angular resolution of the ^{13}CO image is 0.″28 × 0.″21 (40 au × 30 au). The C^{18}O 3–2 data were centered on 329.331 GHz, with 1967 channels of 122.06 kHz (0.111 km s^{-1}) channel width. The angular resolution of the C^{18}O image is 0.″30 × 0.″23 (41 au × 32 au). The dust continuum observation consists of four spectral windows (334.01 ∼ 335.99 GHz, 339.02 ∼ 341.00 GHz, 341.02 ∼ 343.00 GHz, and 346.01 ∼ 347.99 GHz). Each spectral window has 64 channels of 31248.22 kHz (3527.09 km s^{-1}) channel width. The angular resolution of the dust continuum image is 0.″23 × 0.″17 (32 au × 23 au).

This is the first comprehensive observation of the CO 3–2 line emission of ^{12}CO, ^{13}CO, and C^{18}O in the LkCa 15 disk. Previous observations revealed the line emission of various molecules in the LkCa 15 disk, including ^{12}CO 6–5 (van der Marel et al. 2015), CO 2–1, and HCO$^+$ (Qi et al. 2003; Piétu et al. 2007; Punzi et al. 2015); S-bearing molecules (Dutrey et al. 2011); and ethynyl radical (CCH); Henning et al. 2010). The ^{12}CO 2–1 line emission shows that the LkCa 15 disk is highly optically thick in ^{12}CO (Punzi et al. 2015), and the ^{12}CO 6–5 emission shows that gas is still present inside the observed dust cavity (van der Marel et al. 2015). The dust continuum image has also been obtained by several former millimeter observations (Piétu et al. 2006; Espaillat et al. 2007; Isella et al. 2012, 2014), and all of these observations show an inner dust cavity of ∼40–50 au in size.

2.1. Dust Continuum and Line Maps

Figure 1 shows the dust continuum and the ^{12}CO zero-moment maps of the LkCa 15 system. We will extract an azimuthal-averaged flux from these zero-moment maps along the radial direction and use the derived ^{12}CO radial intensity profile as a reference to judge the goodness-of-fit of our disk models. The dust continuum map shows an inner hole of ∼65 au in radius, and the FWHM of this dust cavity is at ∼40 au. This is in agreement with previous millimeter observations (Andrews et al. 2011; Isella et al. 2012, 2014). Such a large inner cavity disappears in the zero-moment map of ^{12}CO. For the optically thin ^{13}CO and C^{18}O emissions, the inner disk show an obvious decrease in the azimuthal-averaged flux. The zero-moment maps of ^{12}CO, ^{13}CO, and C^{18}O are consistent with previous findings that the LkCa 15 disk is optically thick in ^{12}CO emission, while it is optically thin in ^{13}CO and C^{18}O.

Figure 2 shows the observed channel maps of ^{12}CO, ^{13}CO, and C^{18}O of the LkCa 15 disk. The channel maps of ^{12}CO clearly show the near and far halves of a double cone structure, which is the feature resulted from a circular Keplerian rotational disk (Rosenfeld et al. 2013). However, we do not observe such a feature in the channel maps of the optically thin ^{13}CO and C^{18}O due to lower masses of these two isotopes.

3. Modeling

3.1. Surface Density Profile and Parameter Grid

Our primary goal here is to find a gas disk surface density profile that can best reproduce the observed zero-moment ^{12}CO map. First, we create a parameter space by parameterizing the surface density equation of an analytical disk model. Then, we search the parameter space to obtain the best-fit model that has the least-reduced χ^2 of the radial intensity profile of ^{12}CO emission.

The observed radial intensity profiles of CO isotopes and dust continuum emission in the LkCa 15 disk were obtained by extracting the azimuthal-averaged intensity of the zero-moment maps shown in Figure 1. The radial intensity profiles of CO are extended to ∼600 au, while the dust continuum emission shows a ring-shaped structure and ends at ∼200 au. The dust continuum and the CO line emissions cannot be fitted using a single surface density profile. Thus, we use two separate equations to describe the surface density profiles of dust and gas in the LkCa 15 disk.

We employ parameterized analytical disk surface density profiles to model the gas and dust in the LkCa 15 disk. For the gas, we adopt a surface density profile that is described by

$$\Sigma_g(r) = \Sigma_0\left(\frac{r}{\mathrm{RC}}\right)^{-\gamma} \arctan\,(r/\mathrm{RC}_{\mathrm{arctan}})^{\gamma_{\mathrm{arctan}}}, \tag{1}$$

which is a simple power-law density profile combined with an inner cavity described by an arctangent function. We turn off the exponential decay term that is typically used to describe the surface density of protoplanetary disks (e.g., Andrews et al. 2009) because the intensity of CO line emissions decrease slowly at larger radii. Moreover, we fix the characteristic radius (RC) at 12,500 au to slow down the decrease of the gas density at the outer part of the disk. There are four free parameters in Equation (1): Σ_0 determines the disk mass, γ; the power-law decay of the surface density in the radial direction, RC$_{\mathrm{arctan}}$; the size of the inner cavity; and the slope of the junction region between the inner cavity and the outer disk, γ_{arctan}. We set up a four-dimensional parameter space of these four free parameters. The parameter grids at each dimension are listed in Table 1.

The dust surface density profile is described by

$$\Sigma_d(r) = \Sigma_0\left(\frac{r}{\mathrm{RC}}\right)^{-\gamma} \times \exp[-(r/\mathrm{RC})^{2-\gamma}]\arctan\,(r/\mathrm{RC}_{\mathrm{arctan}})^{\gamma_{\mathrm{arctan}}}. \tag{2}$$

Compared with the surface density profile of the gas disk, there is an exponential decay term in the dust density profile to simulate the disappearance of the dust intensity at larger radii. Since we have to subtract the dust continuum emission generating the ^{12}CO images for all the models in the parameter space listed in Table 1, we adopt a fixed dust density profile of RC = 66 au, $\gamma = -0.15$, RC$_{\mathrm{arctan}}$ = 66 au, $\gamma_{\mathrm{arctan}} = 5.35$, and a total dust mass of $M_{\mathrm{dust}} = 9.8 \times 10^{-5}\,M_{\odot}$. These values are determined by fitting the azimuthal-averaged radial intensity profile of the observed dust continuum map, and they are used for all the 4096 runs in the parameter space.

3.2. Physical Model

The first step to derive the ^{12}CO intensity from a specific gas surface density profile is to calculate the three-dimensional disk temperature structure. For each gas surface density profile in the parameter space, we use an iterative approach to obtain a self-consistent three-dimensional disk temperature structure. We assume the disk temperature structure is controlled by micron-size dust particles that are well coupled with gas. Since the vertical distribution of micron-size dust is in turn determined by the disk temperature structure, this is a circular dependency problem. To solve this problem, first we generate an initial three-dimensional micron-size dust distribution and calculate an initial disk temperature based on this dust distribution. Using the calculated disk temperature, we produce a new micron-size dust distribution by solving the differential equation of hydrostatic equilibrium:

$$-\frac{\partial \ln \rho_{\mathrm{gas}}}{\partial z} = \frac{\partial \ln T_{\mathrm{gas}}}{\partial z} + \frac{1}{c_s{}^2}\left[\frac{GM_{*}z}{(r^2+z^2)^{3/2}}\right], \tag{3}$$

where $c_s{}^2 = k_B T_{\mathrm{gas}}/\mu m_h$ is the sound speed. We then run a Monte Carlo radiation transfer simulation to calculate a new disk temperature structure using the updated dust distribution. We repeat this process until the three-dimensional disk temperature structure used to generate a dust distribution and the disk temperature structure calculated by the same dust distribution converge (the difference between the two temperature structures is within 3% everywhere).

The disk temperature structure and the dust continuum and CO line maps are calculated using the Monte Carlo radiative transfer code RADMC-3D (Dullemond 2012). We assume the host star of LkCa 15 is a blackbody radiator with an effective temperature of 4350 K. The surface density of micron-size dust in the calculation of the disk temperature profile is obtained by a dust-to-gas ratio of 0.001. Compared to the Milky Way average ratio of 0.01 (Bohlin et al. 1978), by setting such a small dust-to-gas ratio, we assume that substantial grain growth has occurred in the LkCa 15 disk and the micron-size dust is about 10% in mass of the total dust. Submillimeter and dust continuum observations show that dust grain growth to mm-size particles is completed within less than 1 Myr for the majority of circumstellar disks (Draine 2006; Rodmann et al. 2006; Ricci et al. 2010a, 2010b, 2011; Ubach et al. 2012), and simulation of dust evolution also shows that mm-size dust can form at the age of ∼1 Myr at the high-density region in the protoplanetary disk (Ormel et al. 2009). As aforementioned, the LkCa 15 disk is about 2–5 Myr in age (Kenyon & Hartmann 1995; Simon et al. 2000), thus a large fraction of dust can appear to have large sizes at this stage. The dust opacities used in this work were calculated similar to that of Isella et al. (2009). We assume the dust grains are compact spheres made of astronomical silicates (Weingartner & Draine 2001), organic carbonates (Zubko et al. 1996), and water ice, with fractional abundances described in Pollack et al. (1994). Single-grain opacities were averaged on a grain-size

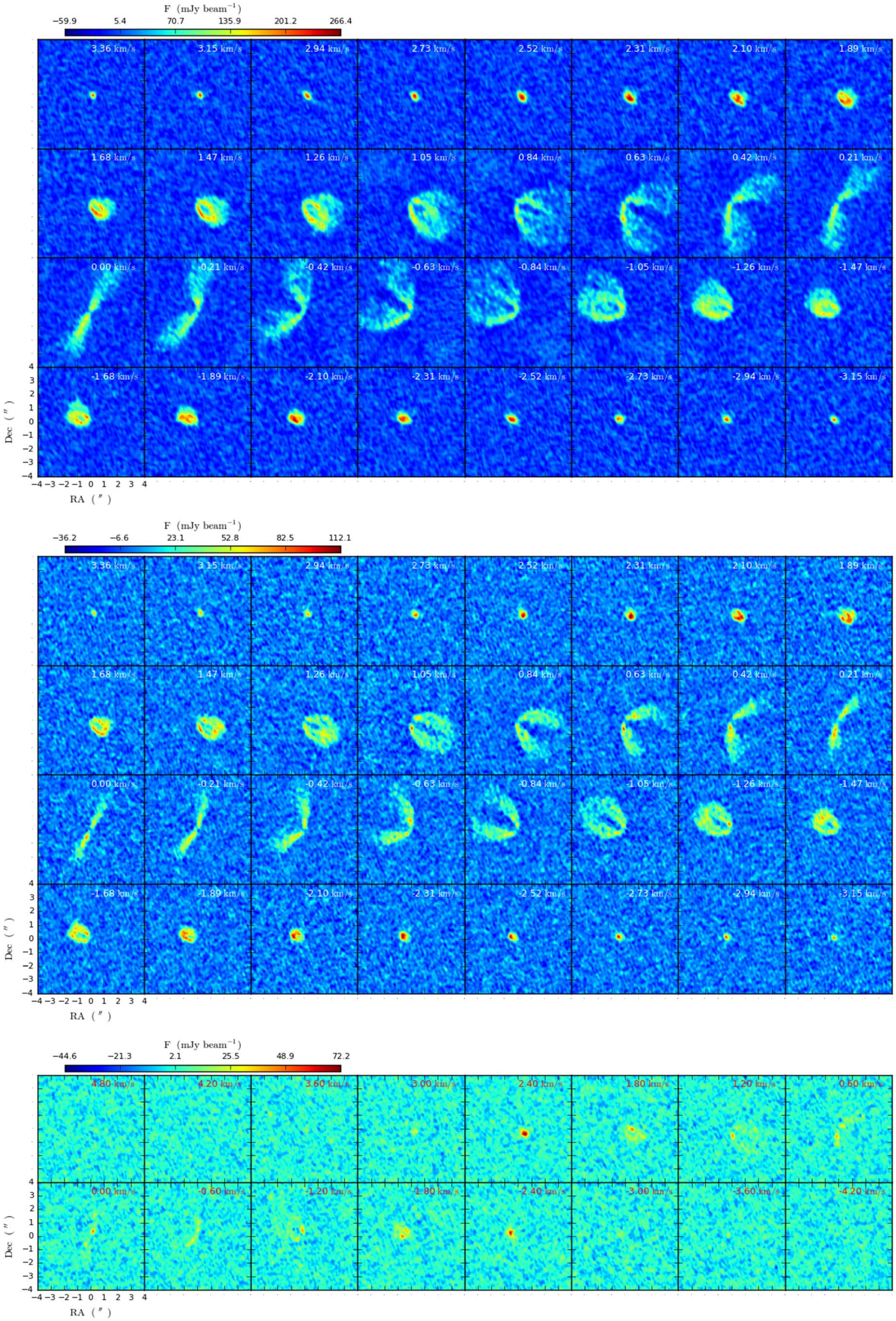

Figure 2. Observed channel maps of ^{12}CO, ^{13}CO, and C^{18}O of the LkCa 15 system.

Table 1
Four-dimensional Parameter Grids

Parameter	Grids
$M_{\rm disk}$ ($M_\odot$)	[1.0e-4, 3.3e-4, 1.0e-3, 3.3e-3, 1.0e-2, 3.3e-2, 1.0e-1, 3.3e-1]
γ	[0.5, 1.0, 2.0, 3.0, 4.0, 5.0, 6.0, 7.0]
$\rm RC_{arctan}$	[1, 5, 15, 25, 35, 45, 55, 65]
$\gamma_{\rm arctan}$	[2, 4, 6, 8, 10, 12, 14, 16]

distribution to obtain the mean opacity. We adopt a typical Mathis et al. 1977 power-law size distribution, $n(a) \propto a^{-3.5}$, between a minimum grain size of 5×10^{-6} mm and a maximum grain size of 1×10^{-2} mm. The resulting dust opacity at the wavelength of 1 μm is 5.2×10^3 cm^2 g^{-1}.

After we have obtained a self-consistent three-dimensional disk temperature structure, we calculate the dust continuum and ^{12}CO line emission. We interpolate the surface density profile of mm-size dust given by Equation (2) on a three-dimensional spherical grid with a scale height profile of $h_{\rm mm\text{-}dust}(r) = 0.1 \times 1.0\,{\rm au} \times (r/20\,{\rm au})^{1.25}$, where 0.1 is a parameter that accounts for the settling of 0.15 mm size dust toward the midplane. This results in a scale height of ∼0.75 au at 100 au for relatively large dust particles. Such a scale height is consistent with the findings of Pinte et al. (2016). The dust opacity adopted for mm-size dust is calculated using the same model of the opacity for micron-size dust; the only difference is that here the maximum grain size is 1 mm. The resulting dust opacity at the wavelength of 1 mm is 13.2 cm^2 g^{-1}. We convolve the dust continuum map in each model with the point-spread function (PSF) of the ALMA observation and extract an azimuthal-averaged radial intensity profile. Then, we calculate the reduced χ^2 for dust continuum emission between the radial intensity profiles of the model and the ALMA observation. For different models in our parameter space, the goodness-of-fit of the dust continuum emission changes due to the variation of the disk temperature. But we find that the influence of the dust continuum map on the zero-moment ^{12}CO map is limited, because the dust continuum image has a ring-like structure that located at the optically thick region of the ^{12}CO emission.

To calculate the line emission of ^{12}CO, we assume the abundance ratio of $^{12}{\rm CO/H_2}$ to be 1.4×10^{-4} in mass, and this value is consistent with the canonical ratio of 10^4 for the disk initial conditions (Lacy et al. 1994; France et al. 2014). Then, we create a three-dimensional density structure of ^{12}CO based on the gas surface density profile of each run by solving Equation (3). We include the freeze-out effect of CO by setting the number density of ^{12}CO to zero at the region where the temperature is below 20 K. Photodissociation by stellar UV and/or X-ray radiation is another important factor as it can destroy the CO in the surface layers of the disk (Visser et al. 2009). We follow the same procedure as in that of Qi et al. (2011) and Rosenfeld et al. (2013), in which we calculate a photodissociation boundary by vertically integrating the H nuclei density to a threshold density of 2.0×10^{20}. This is a mild threshold compared to the value of 5.0×10^{20} used in Rosenfeld et al. (2013). We find that it is hard to fit the ^{12}CO intensity beyond ∼400 au using a larger photodissociation threshold like 5.0×10^{20} in H nuclei, because with such a strong photodissociation rate, there is little ^{12}CO in the outer disk. The photodissociation threshold turns out to be an alternative free parameter in the fitting of the ^{12}CO radial intensity profile, as it is a critical parameter for the ^{12}CO intensity in the outer disk. In this work, we fix the photodissociation threshold of 2.0×10^{20} for all the 4096 runs.

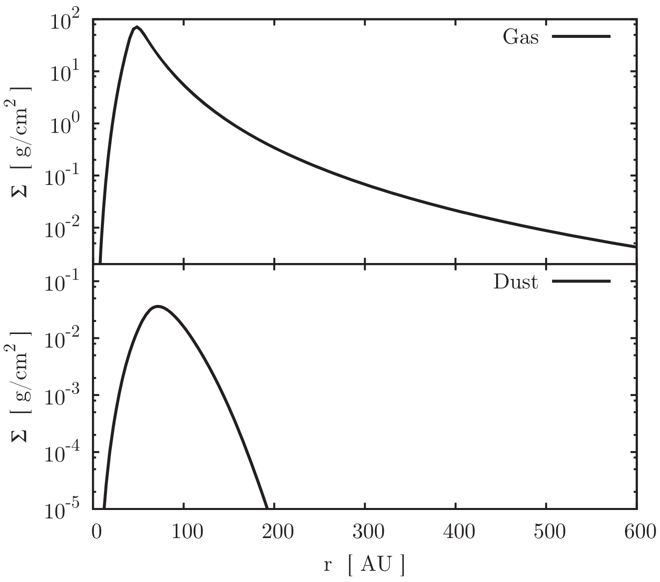

Figure 3. Gas surface density profile of the best-fit run (top panel) and the surface density profile of mm-size dust used in all the 4096 runs (bottom panel).

We first calculate the self-consistent disk temperature. Then, we calculate the dust continuum map and the channel maps of ^{12}CO and convolve these images with the corresponding ALMA PSFs. Afterward, we subtract the dust continuum map from each channel map and integrate all the channel maps to generate a zero-moment map of ^{12}CO. Finally, we subtract an azimuthal-averaged radial intensity profile from the zero-moment ^{12}CO map and calculate the corresponding reduced χ^2 of ^{12}CO emission.

In addition, once we obtain the best-fit parameter sets for the ^{12}CO emission, we tentatively adjust the abundance ratio of $^{12}{\rm CO}/^{13}{\rm CO}$ to fit the radial intensity profile of ^{13}CO, using the same disk temperature profile given by the best-fit ^{12}CO model. The observed ^{13}CO radial intensity profile shows a peak at ∼45 au, although there is no such a peak in the radial intensity profile of ^{12}CO (the radial intensity profiles of ^{12}CO and ^{13}CO can be found in Section 4). Hence, we have to adopt different abundance ratios of $^{12}{\rm CO}/^{13}{\rm CO}$ for the disk region inside or outside of 45 au. Although the fitting process of ^{13}CO is not a self-consistent approach, the result can at least be an estimation of the number density of ^{13}CO. We do not model the C^{18}O disk because the signal-to-noise ratio is low and no flux are detected outside of 200 au.

4. The Best-fit Model

4.1. ^{12}CO Intensity Profile

The best-fit model in our parameter space has the following parameters: $M_{\rm disk} = 0.1\,M_\odot$, $\gamma = 4.0$, $\rm RC_{arctan} = 45$ au, and $\gamma_{\rm arctan} = 10$. Although the fitted disk mass is relatively large, it agrees with previous findings (Isella et al. 2012; Huang et al. 2017). Figure 3 shows the gas surface density profile of this best-fit model, which is related to a power-law disk without an exponential decay term that is usually used in the description of protoplanetary disks (e.g., Andrews et al. 2009). Figure 4 gives the self-consistent temperature structure as calculated by our

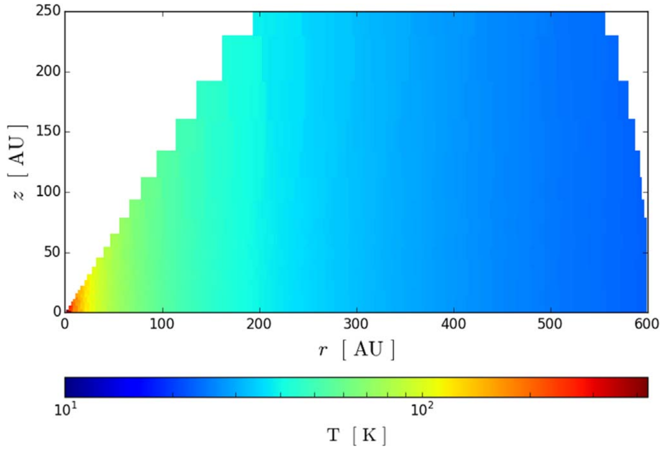

Figure 4. Vertical disk temperature structure of the best-fit model as calculated by our iterative approach.

iterative approach that was described in Section 3.2. It shows a typical two-layer vertical structure of passive irradiated circumstellar disks (Dullemond et al. 2002). In the surface layer, the temperature decreases from ∼51 K at 100 au to ∼29 K at 500 au. In the mid-plane, the temperature decreases from ∼15 K at 100 au to ∼11 K at 500 au.

The top panel of Figure 5 compares the azimuthal-averaged radial intensity profiles extracted from the zero-moment ^{12}CO maps of our best-fit model with the ALMA observation. The best-fit model results in a reduced χ^2 of 2.51. Its gas surface density profile has an inner cavity of 45 au in size. However, we do not see such a cavity in the resulting radial intensity profile, since most of the inner cavity is optically thick in ^{12}CO emission. In fact, for a majority of the gas density profiles in our parameter space, the inner disk region is optically thick in ^{12}CO emission, and its intensity only depends on the calculated disk temperature. Although the very inner part of the disk cavity can become optically thin due to the arctangent function used in the surface density equation, this inner optically thin region did not show up in the radial intensity profile because of the large PSF of the ALMA observation, which is ∼50 au in the major axis and ∼32 au in the minor axis. The observed ^{12}CO intensity decreases slowly in the outer optically thin part of the disk. We find that it is hard to fit the slope of the ^{12}CO radial intensity profile in the entire disk using a simple power-law surface density. Our best-fit model has a large γ of 4.0. It fits the inner ∼400 au very well, but beyond ∼400 au, it shows a lower intensity compared to the ALMA observation. Note that the photodissociation threshold can be another free parameter in our model that can affect the intensity in the outer part of the disk. In order to slow down the decrease of the ^{12}CO intensity beyond ∼400 au, we set a photodissociation threshold of 2.0×10^{20} in H nuclei to keep more ^{12}CO in the outer disk, which is a mild threshold compared to the value of 5.0×10^{20} used in Rosenfeld et al. (2013). Different photodissociation thresholds will result in different best-fit parameter sets.

In Figures 6 and 7, we show the dust continuum map, the ^{12}CO zero-moment map, and the ^{12}CO channel maps of our best-fit model. Rather than interpolating the Fourier transformation of our model images to the actual observation data set and cleaning the data set to get exactly the same PSF of ALMA, we simply convolve a Gaussian function of the same sizes of the major and minor axes with the ALMA observation to speed up our fitting process. Thus, compared to Figures 1 and 2, our model images are smoother than the ALMA observation. For the calculation of reduced χ^2, we only use the azimuthal-averaged intensity profile. We notice that the channel maps provide important constraints on the goodness-of-fit. In the ^{12}CO channel maps shown in Figure 7, we can clearly see the near and far halves of a double cone structure of a Keplerian disk, and the relative angle and magnitude of the near and far halves share similarities with the observed structure shown in Figure 2. These similarities between the channel maps of our best-fit model and the observed channel maps suggest that the mass of LkCa 15 disk is around 0.1 $M_\odot$ under the assumption that the abundance ratio of $^{12}\mathrm{CO}/\mathrm{H}_2$ is $\sim 1.4 \times 10^{-4}$ in mass. The fitting of the outer disk is not good as the disk size is smaller in the channel maps shown in Figure 7, while the observed channel maps in Figure 2 exhibit more extended images. This difficulty is due to the simple power-law surface density profile and the identical radial photodissociation threshold used in our model. We will investigate the effect of different disk masses in Section 5.2. Note that the fitted disk mass depends on the abundance ratio of $^{12}\mathrm{CO}/\mathrm{H}_2$ in our model. If we adopt a larger abundance ratio of $^{12}\mathrm{CO}/\mathrm{H}_2$ of $\sim 3.0 \times 10^{-4}$ in mass, the fitted mass of the LkCa 15 disk should be around 0.05 $M_\odot$.

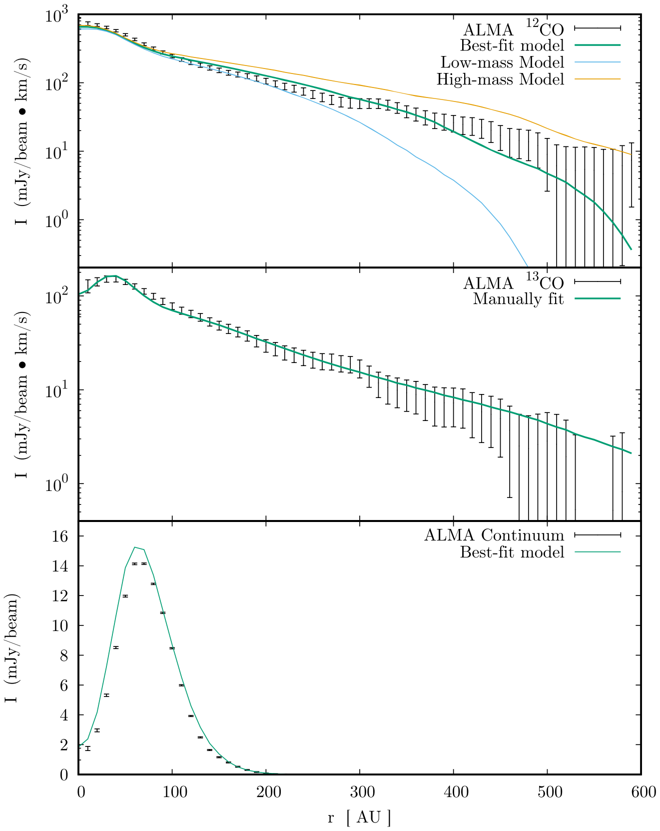

Figure 5. Comparison of the azimuthal-averaged radial intensity profiles that are extracted from the zero-moment maps of ^{12}CO, ^{13}CO, and the dust continuum map. The error bars show the ALMA observation, and the solid green lines show our our best-fit model. The brown and blue lines show the intensity profiles of the high-mass and low-mass models in the parameter study of Section 5.2.

The bottom panel of Figure 5 compares the azimuthal-averaged radial intensity profile of the dust continuum emission

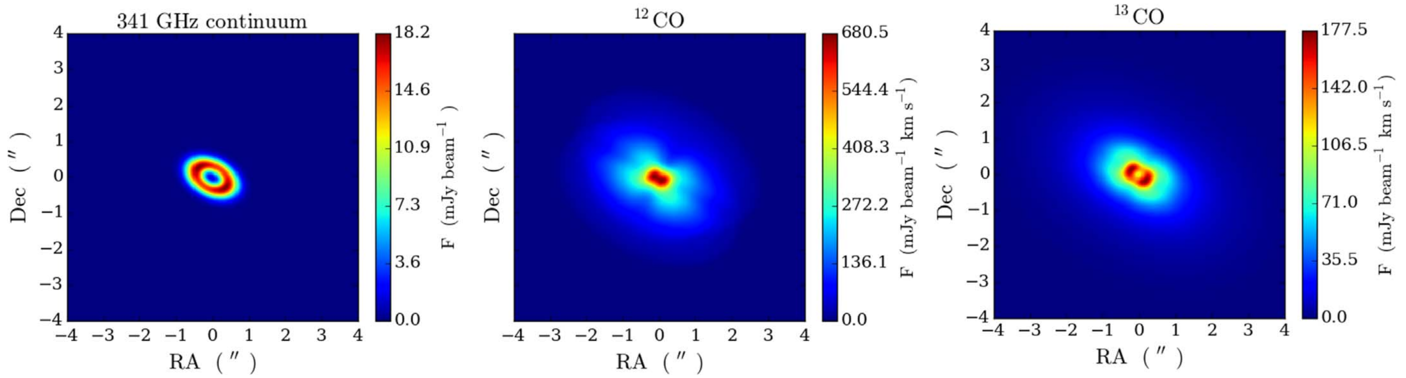

Figure 6. Dust continuum and zero-moment ^{12}CO of our best-fit model and the zero-moment map of the fitted ^{13}CO. Left: dust continuum map. Middle: zero-moment ^{12}CO map. Right: zero-moment ^{13}CO map.

of our best-fit model with the ALMA observation. The observation bias for dust continuum image is small, as shown by the small error bar in the observed radial intensity profile. As a result, the radial intensity profile extracted from the dust continuum image of our best-fit model has a largely reduced χ^2 of 255. But the two intensity profiles of the best-fit model and the ALMA observation generally match. The χ^2 of dust continuum emission can be largely reduced by further fine tuning the dust surface density profile.

4.2. ^{13}CO Image

Based on the surface density profile and the temperature structure of the best-fit model of ^{12}CO, we manually adjust the abundance ratio of ^{12}CO/^{13}CO to fit the observed ^{13}CO intensity. This actually exhibits the ^{13}CO emission at the temperature profile given by the gas density profile obtained by the fitting of ^{12}CO, and it is not a self-consistent way compared to the fitting of the ^{12}CO intensity. We adopt this simplified approach only to estimate the mass of ^{13}CO needed to reproduce the observed ^{13}CO image based on the disk properties of the fitted ^{12}CO disk.

We use a power-law function to describe the radius-dependent abundance ratios of ^{12}CO/^{13}CO:

$$\eta(r) = n_0\left(\frac{r}{45\ \mathrm{au}}\right)^{\alpha}, \tag{4}$$

where $\eta(r)$ is the abundance ratio at r, and n_0 is the abundance ratio at 45 au. We separately fit α for the inner and outer disk regions by manually adjusting n_0 and α. We obtained an n_0 of 6360 and $\alpha = -4.0$ for the disk region inside of 45 au, and $\alpha = 1.7$ outside of 45 au. This leads to ^{12}CO/^{13}CO = 1, 248, and 6360 at 5, 20, and 45 au, and ^{12}CO/^{13}CO = 1640, 500, 155, and 78 at 100, 200, 400, and 600 au. Since the γ in the best-fit ^{12}CO disk is 4, we can infer that the number density profile of ^{13}CO is of the form of $r^{-2.3}$ outside of 45 au. This could partly explain why it is difficult to fit the ^{12}CO intensity in the outer disk using a surface density profile that is of the form of r^{-4}, given that the number density profile fitted from the optically thin ^{13}CO is of $r^{-2.3}$. But if we use a surface density profile that is of the form of $r^{-2.3}$, the fitted disk mass will be around 10^{-3} to $10^{-2}\,M_\odot$ (see Section 5.1 for details). Such a low mass cannot reproduce the morphology of the observed ^{12}CO channel maps as shown in Section 5.2. Thus, it is difficult to fit the ^{12}CO intensity in the inner and outer disk regions using a simple power-law radial density profile. Figure 5 shows the radial intensity profile of ^{13}CO compared with the ALMA observation. The reduced χ^2 of ^{13}CO is derived to be 0.33.

The zero-moment and channel maps of ^{13}CO obtained from the aforementioned fitted abundance ratios are shown in Figures 6 and 7. The fitted zero-moment map of ^{13}CO has an inner cavity, which means the disk becomes optically thin at the wavelengths of ^{13}CO line emissions. The observed zero-moment map of ^{13}CO does not show a distinct inner cavity, but we can see an obvious decrease of the intensity in the inner disk region. For the channel maps, since the mass of ^{13}CO is much lower than the ^{12}CO, we do not see the near and far halves of a double cone structure as shown in the channel maps of ^{12}CO. The morphology of the ^{13}CO channel maps agrees well with the observation.

5. A Parameter Study

5.1. Dependence of Parameters

We aim to investigate how the fitting of the ^{12}CO intensity changes with different parameters. For this, in Figure 8, we plot the heat maps of the reduced χ^2 of the models that have at least two equal parameters with our best-fit model. For example, The top left panel shows the 64 models that have the same $\mathrm{RC}_{\mathrm{arctan}}$ and γ_{arctan} as the best-fit model (marked with a green circle). We see that for the models that have relatively lower reduced χ^2 where they show a clear linear correlation between the M_{disk} and γ. This means that we can find a reasonable fit of the observed ^{12}CO intensity using either a low disk mass with a small γ or a high disk mass with a large γ. This relation can be explained as follows. For most of our 4096 models, the inner part of the disk (inside of ∼300 au) is optically thick for the line emission of ^{12}CO. As a result, the disk temperature profile determines the observed intensity in the inner part of the disk. Since all 64 runs in this panel have the same $\mathrm{RC}_{\mathrm{arctan}}$ and γ_{arctan}, they will have similar disk temperature structures in the inner part of the disk. Thus, the key factor to obtain a good fit for these 64 runs is to derive the right intensity in the outer disk region. This means that in the case of a high-mass disk, we only need to reduce the mass at the outer disk region to obtain a low intensity there to fit the observed ^{12}CO emission. According to Equation (1), to achieve this point, we can set a large γ to decrease the disk surface density quickly at large radii. In Figure 5, we also plot the intensity profiles of two disks that have higher disk masses of

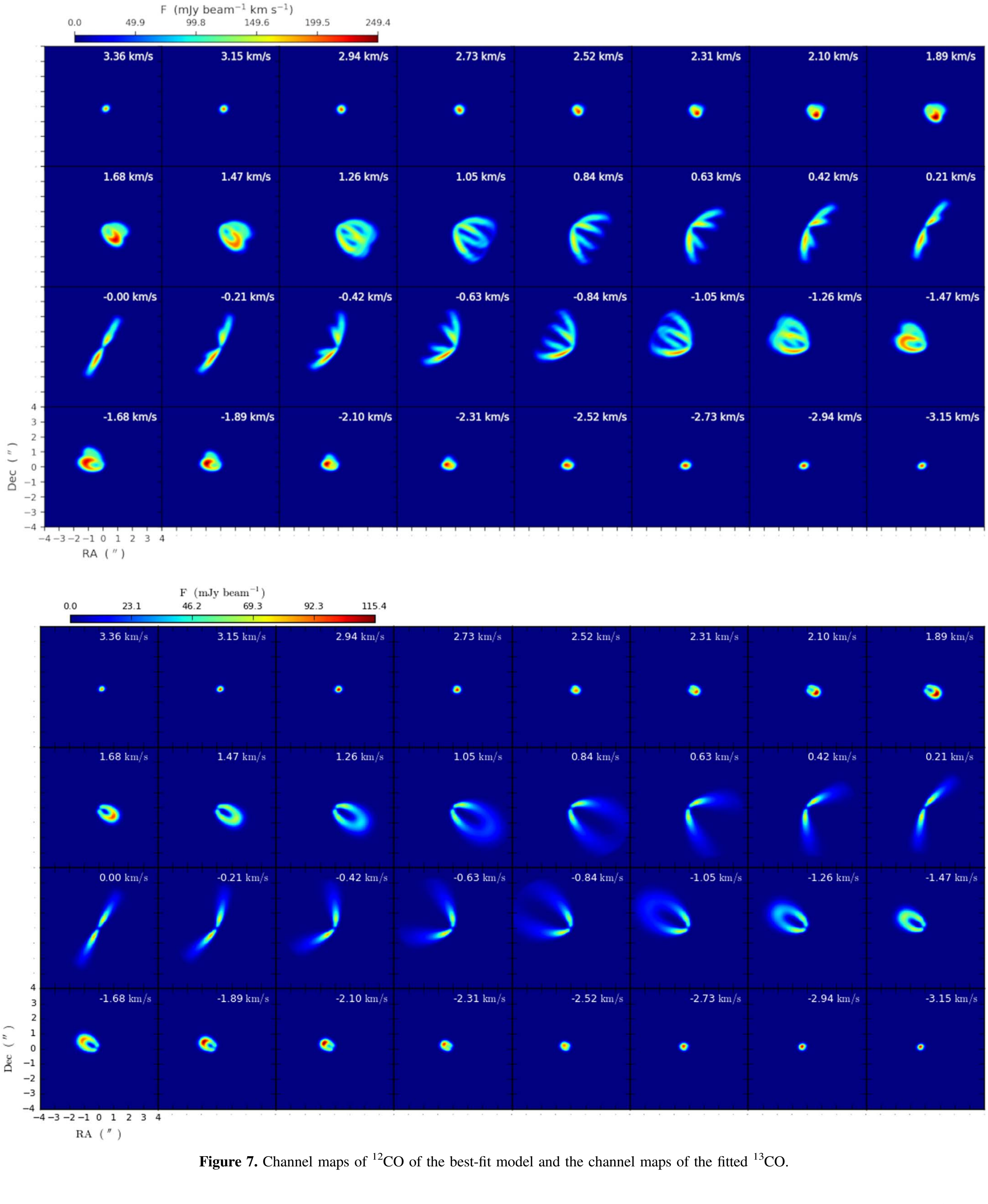

Figure 7. Channel maps of ^{12}CO of the best-fit model and the channel maps of the fitted ^{13}CO.

$0.33\,M_\odot$ or a lower disk masses of $0.033\,M_\odot$, as compared to the best-fit model. The intensity profiles of these three models in the inner 100 au overlap each other. The high-mass model result in a reduced χ^2 of 14.6, and the low-mass model result in a reduced χ^2 of 6.7. The difference between three models is the goodness-of-fit at the outer disk region. We will show in Section 5.2 that the goodness of these three models can also be clearly observed in the morphology of the ^{12}CO channel maps.

The top right panel of Figure 8 shows the 64 models that have the same γ and $\gamma_{\rm arctan}$ with our best-fit model. This panel

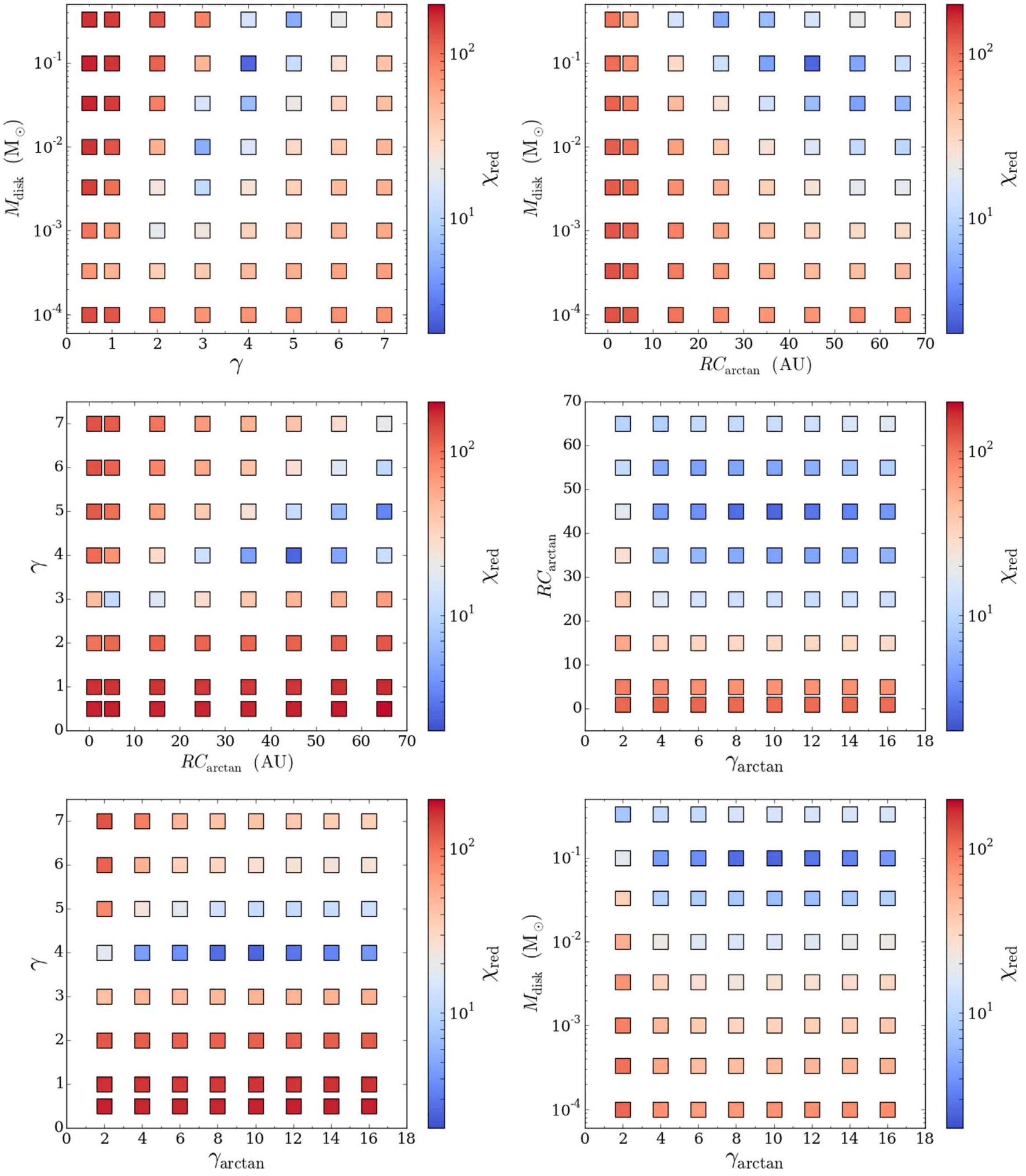

Figure 8. Heat maps of the reduced χ^2 of ^{12}CO in different combinations of parameters.

shows that for the disks that have a small inner cavity (with size $<$10 au), they cannot reproduce the observed ^{12}CO intensity. Only models that have an inner cavity of $\sim$30–60 au can possibly obtain a small reduced χ^2. Furthermore, we can see in the case where the γ, $\gamma_{\rm arctan}$, and $M_{\rm disk}$ are fixed, that the goodness-of-fit shows weak correlation to the size of the inner cavity (RC$_{\rm arctan}$). On the other hand, when the γ, $\gamma_{\rm arctan}$, and RC$_{\rm arctan}$ are fixed, the goodness-of-fit shows weak correlation to the disk mass, since the ^{12}CO emission is optically thick.

The middle left panel of Figure 8 shows the 64 models that have the same $M_{\rm disk}$ and $\gamma_{\rm arctan}$ with the best-fit model. The row with $\gamma = 4$ shows again that the size of the inner cavity plays a less important role in the goodness-of-fit. The essential part in the fitting of the ^{12}CO intensity is to find a combination of γ and $M_{\rm disk}$ that can fit the outer part of the disk. If this goal is achieved, then we can obtain a model that fits the observation, regardless small changes in $\gamma_{\rm arctan}$ and RC$_{\rm arctan}$.

The middle right panel of Figure 8 shows how the reduced χ^2 depends on $\gamma_{\rm arctan}$ and RC$_{\rm arctan}$, i.e., the size of the inner cavity and the slope of the connection region between the inner cavity and outer disk. It confirms that these two parameters have a weak effect on the goodness-of-fit of the ^{12}CO intensity. However, there should be a large inner cavity. It shows that an inner cavity of size $<$20 au does not reproduce the observed ^{12}CO intensity.

The bottom two panels of Figure 8 shows how the reduced χ^2 changes in the γ versus $\gamma_{\rm arctan}$ space and the $M_{\rm disk}$ versus $\gamma_{\rm arctan}$ space. The left panel shows that if the $M_{\rm disk}$ is fixed, then

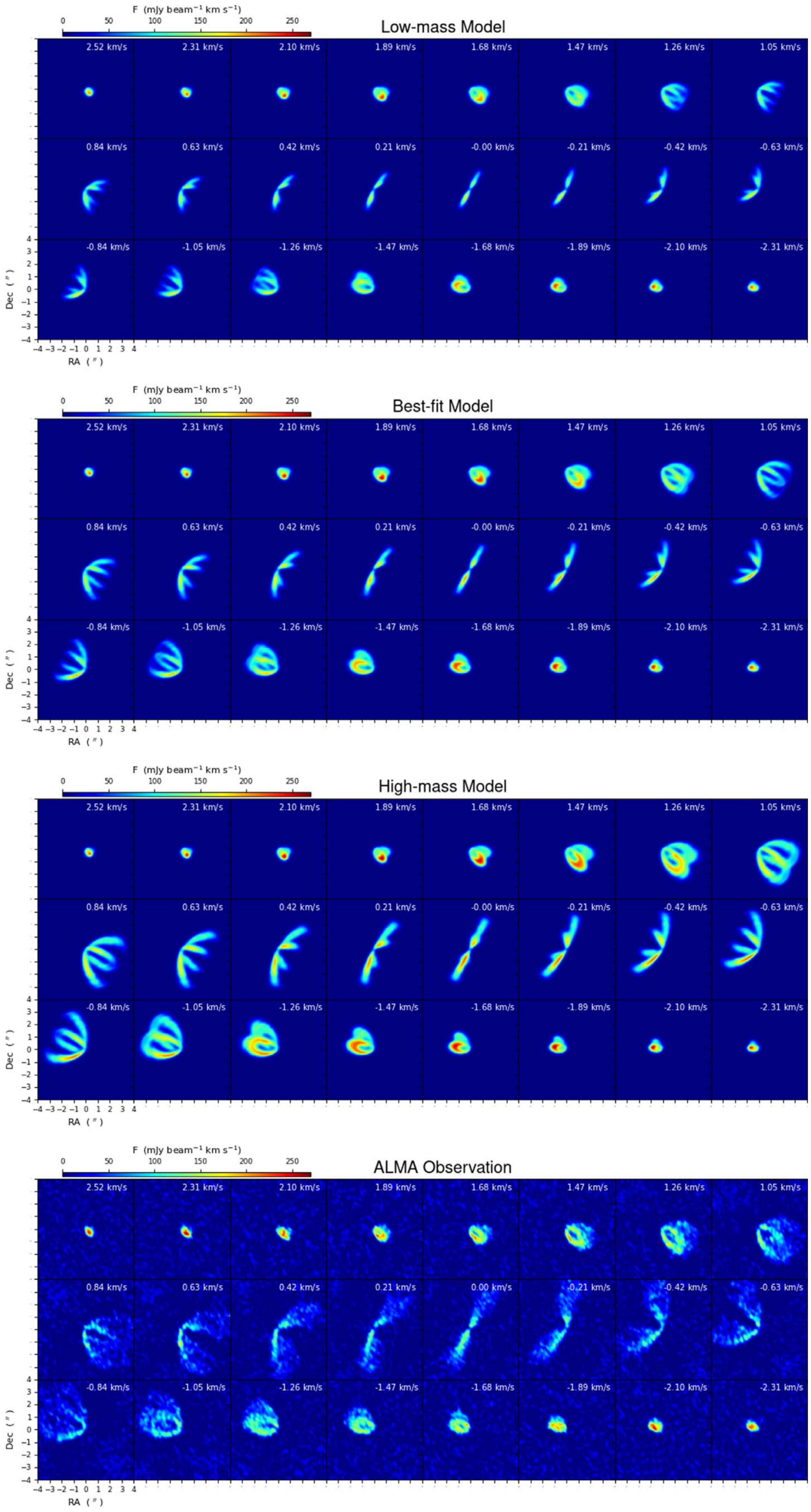
Low-mass Model

Best-fit Model

High-mass Model

ALMA Observation

Figure 9. ^{12}CO channel maps of the low-mass, best-fit, and high-mass models and the ALMA observation.

the γ determines the goodness-of-fit. On the contrary, the right panel shows that if the γ is fixed, the $M_{\rm disk}$ determines the goodness-of-fit. For $\gamma_{\rm arctan}$, here we see again that it has a very limited effect on the goodness-of-fit. Therefore, we may conclude that the most important part in obtaining a good fit is to find a combination of $M_{\rm disk}$ and γ.

5.2. Constraint on the Disk Mass

The best-fit model in our parameter space has a disk mass of $0.1\,M_\odot$, a γ of 4.0, and an inner cavity of 45 au. We have seen in Section 5.1 that the goodness-of-fit is affected by different combination of parameters, as the top left panel in Figure 8 shows that by adjusting the γ, we can obtain reasonable fits with higher or lower disk masses. Here, we investigate how much our model constrains the mass of the LkCa 15 disk. We choose three models from the top left panel in Figure 8: the best-fit model, a high-mass disk model of $0.33\,M_\odot$, and a low-mass model of $0.033\,M_\odot$ (these three models are marked with a green, brown, and blue circle, respectively). The radial intensity profiles of three models are shown in Figure 5, and the high-mass or low-mass models either overproduce or underproduce the intensity out of ∼100 au. Since the radial intensity profile is extracted from the zero-moment map that is actually a degenerated image obtained by combining all the channel maps in an actual observation, we expect that the difference of these models can also be observed in the channel maps.

In Figure 9, we compare the three models' channel maps with the ALMA observation, where all the channel maps are plotted in the same color bar. The most apparent difference between three models is the size of the channel maps. Since we have seen in Figure 5 that the high-mass and low-mass models result in either higher or lower intensities in the outer part of the disk, they either show larger or smaller sizes in the channel maps compared with the best-fit model. There is another feature that can be used as an effective criteria for the goodness-of-fit of the disk mass, i.e., the morphology of the near and far halves of a double cone structure of a Keplerian disk. For example, in the channel map at the velocity of $\pm1.05\,{\rm km\,s^{-1}}$, the high-mass model shows a too-intense far half in the double cone structure compared to the observation, while the low-mass model shows a much smaller double cone structure since it underproduce the intensity at the outer disk region. In the channel maps, at velocities of ±0.63 and $\pm0.42\,{\rm km\,s^{-1}}$, the two short wings of the double cone structure in the high-mass model are too strong compared to the observation. Thus, the inability of the high-mass and low-mass models to fit the intensity in the outer disk region also exhibits in the morphology of the double cone structure in the channel maps. They show a double cone structure that is either too strong or too weak compared to the observed channel maps.

The mm-size dust surface density profile that can reproduce the observed dust continuum map is significantly different compared to the fitted gas surface density profile, and this is a reliable result because of the small observational bias of the dust continuum emission. The mm-size dust density profile has a peak at ∼65 au, indicating a pressure bump exists at the same location in the gas disk. The FWHM of this dust cavity is at ∼40 au, which is similar to the inner cavity of the fitted gas disk. The mm-size dust disk has an outer edge at ∼200 au, which is much smaller compared to the fitted gas disk of ∼600 au in size. Such a discrepancy between the gas and dust disks provides an important constraint of the dust drifting models in the LkCa 15 system. Our mm-size dust disk is $\sim1.0\times10^{-4}\,M_\odot$ in mass. According to our dust opacity model, the opacity at the mm wavelength is mainly contributed by dust of ∼0.15 mm in size. This suggests a dust-to-gas ratio of ∼0.001 for dust of ∼0.15 mm in size. But this is a weak constraint because we adopt a uniform opacity model for dust at different distances. In reality, the species and the size distribution of dust should change at different radii, and this will affect the calculated dust opacity and, consequently, the fitted dust masses at different radii.

6. Conclusions

In this work, we analyze the dust continuum and ^{12}CO 3–2 line emission maps of the LkCa 15 disk that are obtained from ALMA observation. We parameterize an analytical surface density profile of the LkCa 15 disk and search through the parameter space to find the best-fit gas surface density model that leads to the least-reduced χ^2 of the ^{12}CO intensity. Our key findings are summarized as follows:

1. The best-fit model of the gas disk based on ^{12}CO 3–2 line emission is a disk of $0.1\,M_\odot$ in mass. The gas disk has an inner cavity of 45 au in size, and its outer edge is at ∼600 au. The surface density profile of this best-fit model follows a power-law of the form of $\rho_r \propto r^{-4}$. But such a steep power-law density profile results in a lower ^{12}CO intensity at the outer part of the disk beyond ∼400 au compared to the observation.
2. The dust continuum map can be reproduced by a dust disk that has an inner cavity of ∼65 au in size, and the FWHM of this cavity is ∼40 au. The size of the dust cavity is similar to the size of the fitted gas cavity. Unlike the gas disk, the mm-size dust disk ends at ∼200 au. The discrepancy between the outer edges of the gas and dust disks can be used to study the dust drifting models in the LkCa 15 disk.
3. The heat maps of the reduced χ^2 of different models show a linear correlation between $M_{\rm disk}$ and γ for the models that have a reasonable goodness-of-fit of the radial intensity profile of ^{12}CO. This means that we can fit the observed ^{12}CO intensity using either a lower disk mass with a smaller γ or a higher disk mass with a bigger γ. Because the inner disk region is optically thick, the key factor to derive a good fit is to adjust the density profile in the outer disk region to obtain consistent intensity there.
4. The morphologies of the ^{12}CO channel maps are important constraints of the disk mass. In our parameter space, although there are some models with higher or lower disk masses that can result in a reasonable reduced χ^2, their channel maps show a double cone structure that is either too strong or too weak compared to the ALMA observation. The best-fit model with a disk mass of $\sim0.1\,M_\odot$ can best reproduce the observed channel maps.

This paper makes use of the following ALMA data: ADS/JAO.ALMA No. 2012.1.00870.S. ALMA is a partnership of ESO (representing its member states), NSF (USA), and NINS (Japan), together with NRC (Canada), MOST, and ASIAA (Taiwan), and KASI (Republic of Korea), in cooperation with the Republic of Chile. The Joint ALMA Observatory is operated by ESO, AUI/NRAO, and NAOJ. S.J. and J.J. acknowledge support from the National Natural Science Foundation of China (grant Nos. 11503092, 11773081, 11661161013, 11573073, and 11633009), the CAS Interdisciplinary Innovation Team, the Strategic Priority Research Program on Space Science, the

Chinese Academy of Sciences (grant No. XDA15020302), and the Foundation of Minor Planets of Purple Mountain Observatory. A.I. acknowledges support from the National Science Foundation through grant No. AST-1715719 and the National Aeronautics and Space Administration support from the National Aeronautics and Space Administration through grant No. 80HQTR18T0061 and the Center for Space and Earth Science at LANL. We thank the referee for comments that helped to improve the manuscript.

Software: RADMC-3D v0.41 (Dullemond 2012), CASA ALMA pipeline 5.4.0.

ORCID iDs

Sheng Jin https://orcid.org/0000-0002-9063-5987
Andrea Isella https://orcid.org/0000-0001-8061-2207
Pinghui Huang https://orcid.org/0000-0002-7575-3176
Shengtai Li https://orcid.org/0000-0002-4142-3080
Hui Li https://orcid.org/0000-0003-3556-6568
Jianghui Ji https://orcid.org/0000-0002-9260-1537

References

ALMA Partnership, Brogan, C. L., Pérez, L. M., et al. 2015, ApJL, 808, L3
Andrews, S. M., Huang, J., Pérez, L. M., et al. 2018, ApJL, 869, L41
Andrews, S. M., Rosenfeld, K. A., Wilner, D. J., & Bremer, M. 2011, ApJL, 742, L5
Andrews, S. M., Wilner, D. J., Hughes, A. M., Qi, C., & Dullemond, C. P. 2009, ApJ, 700, 1502
Birnstiel, T., Dullemond, C. P., & Brauer, F. 2010, A&A, 513, A79
Bohlin, R. C., Savage, B. D., & Drake, J. F. 1978, ApJ, 224, 132
Chapillon, E., Guilloteau, S., Dutrey, A., & Piétu, V. 2008, A&A, 488, 565
Currie, T., Marois, C., Cieza, L., et al. 2019, ApJL, 877, L3
Dong, R., Li, S., Chiang, E., & Li, H. 2018, ApJ, 866, 110
Dong, R., Zhu, Z., & Whitney, B. 2015, ApJ, 809, 93
Draine, B. T. 2006, ApJ, 636, 1114
Dullemond, C. P., Juhasz, A., Pohl, A., et al. 2012, RADMC-3D: A multi-purpose radiative transfer tool, Astrophysics Source Code Library, ascl:1202.015
Dullemond, C. P., van Zadelhoff, G. J., & Natta, A. 2002, A&A, 389, 464
Dutrey, A., Wakelam, V., Boehler, Y., et al. 2011, A&A, 535, A104
Espaillat, C., Calvet, N., D'Alessio, P., et al. 2007, ApJL, 670, L135
Fedele, D., Carney, M., Hogerheijde, M. R., et al. 2017, A&A, 600, A72
France, K., Herczeg, G. J., McJunkin, M., et al. 2014, ApJ, 794, 160
Hartmann, L., Calvet, N., Gullbring, E., & D'Alessio, P. 1998, ApJ, 495, 385
Henning, T., Semenov, D., Guilloteau, S., et al. 2010, ApJ, 714, 1511
Huang, J., Öberg, K. I., Qi, C., et al. 2017, ApJ, 835, 231
Huang, P., Isella, A., Li, H., Li, S., & Ji, J. 2018, ApJ, 867, 3
Isella, A., Carpenter, J. M., & Sargent, A. I. 2009, ApJ, 701, 260
Isella, A., Chandler, C. J., Carpenter, J. M., Pérez, L. M., & Ricci, L. 2014, ApJ, 788, 129
Isella, A., Guidi, G., Testi, L., et al. 2016, PhRvL, 117, 251101
Isella, A., Huang, J., Andrews, S. M., et al. 2018, ApJL, 869, L49
Isella, A., Pérez, L. M., & Carpenter, J. M. 2012, ApJ, 747, 136
Jin, S., Li, S., Isella, A., Li, H., & Ji, J. 2016, ApJ, 818, 76
Kenyon, S. J., & Hartmann, L. 1995, ApJS, 101, 117
Kraus, A. L., & Ireland, M. J. 2012, ApJ, 745, 5
Lacy, J. H., Knacke, R., Geballe, T. R., & Tokunaga, A. T. 1994, ApJL, 428, L69
Liu, S.-F., Jin, S., Li, S., Isella, A., & Li, H. 2018a, ApJ, 857, 87
Liu, Y., Dipierro, G., Ragusa, E., et al. 2018b, A&A, 622, A75
Mathis, J. S., Rumpl, W., & Nordsieck, K. H. 1977, ApJ, 217, 425
Öberg, K. I., Qi, C., Fogel, J. K. J., et al. 2010, ApJ, 720, 480
Oh, D., Hashimoto, J., Tamura, M., et al. 2016, PASJ, 68, L3
Ormel, C. W., Paszun, D., Dominik, C., et al. 2009, A&A, 502, 845
Piétu, V., Dutrey, A., & Guilloteau, S. 2007, A&A, 467, 163
Piétu, V., Dutrey, A., Guilloteau, S., Chapillon, E., & Pety, J. 2006, A&A, 460, L43
Pinilla, P., Benisty, M., & Birnstiel, T. 2012, A&A, 545, A81
Pinte, C., Dent, W. R. F., Menard, F., et al. 2016, ApJ, 816, 25
Pollack, J. B., Hollenbach, D., Beckwith, S., et al. 1994, ApJ, 421, 615
Punzi, K. M., Hily-Blant, P., Kastner, J. H., Sacco, G. G., & Forveille, T. 2015, ApJ, 805, 147
Qi, C., D'Alessio, P., Öberg, K. I., et al. 2011, ApJ, 740, 84
Qi, C., Kessler, J. E., Koerner, D. W., et al. 2003, ApJ, 597, 986
Ricci, L., Liu, S.-F., Isella, A., & Li, H. 2018, ApJ, 853, 110
Ricci, L., Mann, R. K., Testi, L., et al. 2011, A&A, 525, A81
Ricci, L., Testi, L., Natta, A., et al. 2010a, A&A, 512, A15
Ricci, L., Testi, L., Natta, A., et al. 2010b, A&A, 521, A66
Rodmann, J., Henning, T., Chandler, C. J., et al. 2006, A&A, 446, 211
Rosenfeld, K. A., Andrews, S. M., Hughes, A. M., Wilner, D. J., & Qi, C. 2013, ApJ, 774, 16
Sallum, S., Follette, K. B., Eisner, J. A., et al. 2015, Natur, 527, 342
Simon, M., Dutrey, A., & Guilloteau, S. 2000, ApJ, 545, 1034
Skinner, S. L., & Güdel, M. 2013, ApJ, 765, 3
Thalmann, C., Grady, C. A., Goto, M., et al. 2010, ApJL, 718, L87
Thalmann, C., Janson, M., Garufi, A., et al. 2016, ApJL, 828, L17
Thalmann, C., Mulders, G. D., Hodapp, K., et al. 2014, A&A, 566, A51
Thalmann, C., Mulders, G. D., Janson, M., et al. 2015, ApJL, 808, L41
Thi, W.-F., van Zadelhoff, G.-J., & van Dishoeck, E. F. 2004, A&A, 425, 955
Ubach, C., Maddison, S. T., Wright, C. M., et al. 2012, MNRAS, 425, 3137
van den Ancker, M. E., de Winter, D., & Tjin A Djie, H. R. E. 1998, A&A, 330, 145
van der Marel, N., van Dishoeck, E. F., Bruderer, S., Pérez, L., & Isella, A. 2015, A&A, 579, A106
Visser, R., van Dishoeck, E. F., & Black, J. H. 2009, A&A, 503, 323
Weingartner, J. C., & Draine, B. T. 2001, ApJ, 548, 296
Zhu, Z., Nelson, R. P., Hartmann, L., Espaillat, C., & Calvet, N. 2011, ApJ, 729, 47
Zubko, V. G., Mennella, V., Colangeli, L., & Bussoletti, E. 1996, MNRAS, 282, 1321